Comparative Evaluation of IPT Resonant Circuit Topologies for Wireless Power Supplies of Implantable Mechanical Circulatory Support Systems

Author(s):
Knecht, Oliver; Kolar, Johann W.

Publication date:
2017-03

Permanent link:
https://doi.org/10.3929/ethz-b-000130828

Originally published in:
https://doi.org/10.1109/APEC.2017.7931166

Comparative Evaluation of IPT Resonant Circuit Topologies for Wireless Power Supplies of Implantable Mechanical Circulatory Support Systems

Oliver Knecht, and Johann W. Kolar
Power Electronic Systems Laboratory, ETH Zürich, Switzerland, e-mail: knecht@lem.ee.ethz.ch

***Abstract*— Today's implantable blood pumps, such as Left Ventricular Assist Devices (LVAD) are powered by means of a percutaneous driveline, which constitutes a severe risk of infection to the patient. Inductive Power Transfer (IPT) technology offers a solution to replace the driveline by a wireless energy link. In this paper, three commonly used IPT resonant circuit topologies are compared regarding power transfer efficiency and heating of the tissue. In the course of the analysis, the main advantages and disadvantages of each topology are identified and as a result it was found that regarding the heating of the tissue, the series-series compensated topology is the most promising solution for Transcutaneous Energy Transfer (TET) systems capable to provide a peak power transmission of up to 30 W. Operated at the resonant frequency using an efficiency optimal control, the series-series compensation topology achieves the highest DC-to-DC power conversion efficiency in the coil coupling and output power range, but requires a higher complexity of the control system, and more important, it shows an increasing secondary side coil power loss with decreasing coil coupling factor. In contrast, the operation near the frequency for load independent voltage gain using a load impedance control technique achieves similar power conversion efficiencies at high coil coupling factors, but offers a lower complexity of the overall TET system. The peak DC-to-DC efficiency measured with a hardware prototype is 97 % at a coil separation distance of 10 mm, a primary and secondary coil diameter of 70 mm and ideal coil alignment. Even at a coil separation distance of 20 mm and an output power of 5 W, the efficiency is 90.5 %.**

***Index Terms*—Transcutaneous energy transfer, inductive power transfer, thermal modeling**

I. Introduction

For patients suffering from end stage heart failure, a heart transplantation is often the only curative treatment. The limited availability of donor organs promoted the development of Mechanical Circulatory Support Systems (MCSS) such as Left Ventricular Assist Devices (LVAD), which help the weakened heart to provide the pump capacity needed to maintain the regular blood circulation in the body. However, the percutaneous driveline that is used today to power the LVAD constitutes a severe risk of infection to the patient [1]. Therefore, Inductive Power Transfer (IPT) technology was deployed as a promising solution for powering the LVAD without the need for a galvanic contact [2].

The basic structure of a typical Transcutaneous Energy Transfer (TET) system is shown in **Fig. 1**. The key part is the IPT system including an inverter, a rectifier and the IPT resonant circuit, including the energy transmission coils. The TET system further contains the power management circuit needed to control the power flow in the IPT system, as well as the charging controller of the secondary side backup battery which allows for a temporary completely untethered operation of the implant. Today's state-of-the-art LVADs have a continuous power consumption of 4-12 W [3], [4]. For bi-ventricular support, the power consumption could be even higher. Hence, the maximum power transfer capability of the TET system considered in this work is in a range of up to 30 W, in order to be able to recharge the backup battery.

In the literature, several implementations of TET systems for mechanical circulatory support [5]–[10] and generally applicable strategies for the optimal design and operation of IPT resonant circuit topologies [11]–[17] are presented, but a direct comparison of the IPT topologies concerning multiple objectives, i.e. the power transfer efficiency and the heating of the tissue and/or the design limitations are not shown for the application at hand. Therefore, in this paper, three commonly used IPT resonant circuit topologies shown in **Fig. 1(a)-(c)**, i.e. the series-series (SS) **(a)**, the series-parallel (SP) **(b)** and the series-series-parallel (SSP) **(c)** compensated topology are compared regarding the power transfer efficiency, the secondary side coil peak voltage and regarding the thermal limitation due to the heating of the tissue. In addition, a distinction is made for the series-series resonant circuit topology, which is designed either for the operation at resonance (referred to as SSR compensation) or for the operation above resonance near the frequency for load-independent voltage gain, which is referred to as SSU compensation [18]. In **Section II** the design of each IPT resonant circuit is summarized and the design equations as well as an accurate equivalent load model for the secondary side parallel compensated IPT systems are shown. In addition, a detailed thermal model for the IPT coils in the human tissue is provided in order to find the thermal limit for each topology. In the course of the discussion, the series-series compensation approach is identified as the most promising IPT resonant circuit topology for the high power transfer capabilities targeted in the application at hand, and in **Section III**, the optimal control for the SSR system [19] is reviewed and compared to the SSU system operation using a load impedance control technique. Concluding remarks are given in **Section IV**.

II. IPT Topology Comparison

A. IPT System Design

The evaluation of the performance of each IPT resonant circuit topology is based on the power loss modeling of the primary and secondary side energy transfer coils, as the losses are on one hand determining the power transfer efficiency and on the other hand the heating of the tissue. Hence, for any IPT coil setup which is defined by the coil geometry, the minimum coil separation distance $d_{\mathrm{c,min}}$ and the operating frequency f_0, the primary and secondary side coil AC resistances and the coil currents must be calculated at the maximum output power $P_{2,\mathrm{max}}$. The dimensioning of each resonant circuit topology is based on the maximization of the power transfer efficiency at maximum output power. It is shown in [2], [20] that the maximum efficiency of the wireless energy transmission link in its simplest form, i.e. considering the power losses in the energy transmission coils only, can be approximated with

$$\eta_{\mathrm{max}} \approx 1 - \frac{2}{k\sqrt{Q_1 Q_2}}\,, \tag{1}$$

with the coil coupling factor k and the coil quality factors given by

$$k = \frac{L_{\mathrm{h}}}{\sqrt{L_1 L_2}} \qquad \text{and} \qquad Q_{\mathrm{i}} = \frac{\omega L_{\mathrm{i}}}{R_{\mathrm{i}}(\omega)} \qquad i \in [1,2]\,, \tag{2}$$

where L_{h} denotes the mutual inductance and Q_1 and Q_2 denote the quality factor of the primary and secondary coil respectively. According to (1), the product $k\sqrt{Q_1 Q_2}$ is a Figure-Of-Merit (FOM) for the energy transmission efficiency. Hence, using coils with high quality factors, i.e. a large ratio between the peak energy stored and the energy dissipated in the coil, it is possible to compensate for the

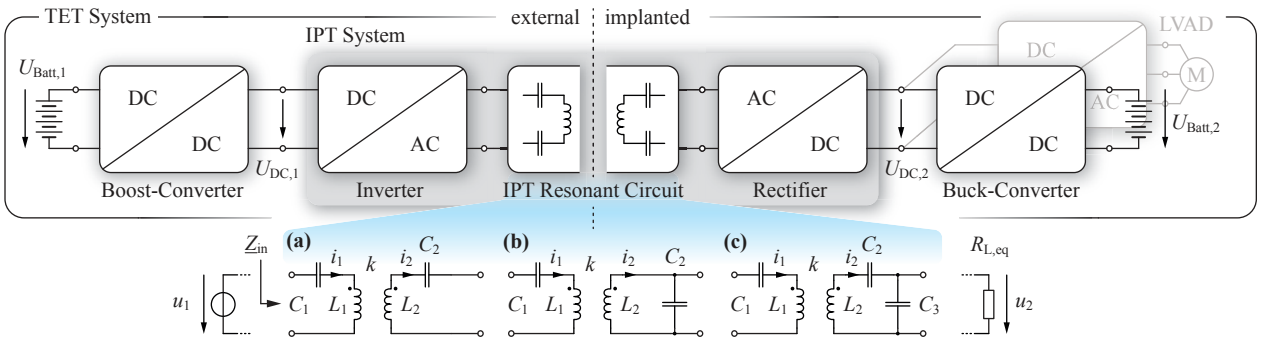

Figure 1: Basic power management concept of the Transcutaneous Energy Transfer (TET) system. (a)-(c) Common implementations of the IPT resonant circuit.

IPT Resonant Circuit	SS Compensation		SP Compensation	SSP Compensation
Operating Frequency	at resonance	at the frequency for load independent voltage gain [1]		
Compensation Capacitors	$C_1 = \frac{1}{\omega_0^2 L_1}$ (SSR) $C_2 = \frac{1}{\omega_0^2 L_2}$	$C_1 = \frac{1}{\omega_0^2 L_1 (1-k_0)}$ (SSU) $C_2 = \frac{1}{\omega_0^2 L_2 (1-k_0)}$	$C_1 = \frac{1}{\omega_0^2 L_1 (1-k_0^2)}$ $C_2 = \frac{1}{\omega_0^2 L_2}$	$C_1 = \frac{1}{\omega_0^2 L_1 (1-k_0)}$ $C_3 = \frac{1}{\omega_0^2 L_2 k_0}$ $C_2 = \frac{1}{\omega_0^2 L_2 (1-k_0)}$
Optimal Load Matching Factor $\gamma_{\mathrm{opt}} = R_{\mathrm{L,eq}} / (\omega_0 L_2)$	$\frac{1}{Q_2}\sqrt{1+k^2 Q_1 Q_2}$	$\frac{1}{Q_2}\sqrt{1+k^2 Q_1 Q_2 + (k_0 Q_2)^2}$	$\sqrt{\frac{1+k^2 Q_1 Q_2 + Q_2^2}{1+k^2 Q_1 Q_2}}$	$k_0\sqrt{\frac{1+k^2 Q_1 Q_2 + (k_0 Q_2)^2}{1+k^2 Q_1 Q_2}}$
Optimal Load Resistance $R_{\mathrm{L,eq,opt}}$ [2]	$\omega_0 L_2 k$	$\omega_0 L_2 \sqrt{k^2 + k_0^2}$	$\omega_0 L_2 \frac{1}{k}\sqrt{1+k^2}$	$\omega_0 L_2 k_0 \sqrt{\frac{k^2+k_0^2}{k^2}}$
Design Coupling Factor k_{d} [3]	$k_{\mathrm{d}} = k_{\max}$	$k_{\mathrm{d}} = k_0 = \frac{k_{\max}}{\sqrt{3}}$	$k_{\mathrm{d}} = k_0 = k_{\max}$	$k_{\mathrm{d}} = k_0 = k_{\max}$

1) can be achieved only for $k = k_{\mathrm{d}}$
2) assuming that Q_1, $Q_2 > 200$
3) the system is designed for $k = k_{\mathrm{d}}$, $P_2 = P_{2,\max}$ and $\omega_0 = 2\pi f_0$

Table I: Inductive Power Transfer (IPT) system design equations.

low magnetic coupling and still achieve a high energy transmission efficiency. The maximum efficiency is then achieved by matching the AC load resistance $R_{\mathrm{L,eq}}$ to the characteristic impedance of the receiver coil [15].

Following the analytical method and the results presented in [15], [17], a set of design equations can be derived for each topology, which is provided in **Tab. I**. The optimal load matching factor γ_{opt} denotes the ratio of the AC load resistance $R_{\mathrm{L,eq}}$ to the impedance of the secondary side coil, which results in the maximum efficiency for the IPT coil set at hand. At high coil quality factors, i.e. factors that exceed a value of 200, the optimal load factor can be simplified [17] and a simple equation of the optimal equivalent AC load resistance $R_{\mathrm{L,opt}}$ can be found for each IPT system topology, as shown in **Tab. I**. In order to design the resonant circuit for this special case where the input impedance $\underline{Z}_{\mathrm{in}}$ is purely resistive, the circuit must be dimensioned for the design coupling factor $k = k_{\mathrm{d}}$ given in **Tab. I** and the operating frequency f_0 and the maximum rated output power $P_{2,\max}$. Except for the SSU system operation, the design coupling factor corresponds to the maximum achievable coupling $k_{\max}$, which is given by the geometric limitations for the application at hand (i.e. the minimum feasible coil separation distance and ideal alignment of the coils). This design procedure guarantees that the input impedance of the IPT resonant circuit is always inductive, i.e. the phase angle of the input impedance $\varphi_{\underline{Z},\mathrm{in}}$ is positive, when $k < k_{\max}$ and $P_2 < P_{2,\max}$ applies, which is a requirement to achieve Zero-Voltage-Switching (ZVS) of the primary side full-bridge class-D inverter stage in the operating range, i.e. in the specified output power and feasible coil coupling range.

Fig. 2 shows the voltage gain $G_{\mathrm{v}}(\mathrm{dB}) = 20\log_{10}(|\underline{u}_2/\underline{u}_1|)$ and phase angle of the input impedance $\varphi_{\underline{Z},\mathrm{in}}$ for each IPT system topology, designed according to the equations provided in **Tab. I**, with a primary side inductance chosen such that the voltage gain is unity at the maximum output power and maximum coupling factor. As depicted in **Fig. 2(a)** and **(b)**, in a practical realization, the SSR and SSU system must be operated at a frequency which is slightly higher than the nominal operating frequency f_0 in order to achieve ZVS at maximum output power and at maximum coil coupling. In contrast, the SP and SSP systems must be operated at a slightly lower operating frequency in order to achieve the same objective.

In order to evaluate a large number of possible designs, a vast number of feasible IPT coil sets was generated in a numerical simulation. The coupling factor and the AC resistance of each coil was calculated as described in [21], based on the analytical models provided in [22]. The parameter range and designation used for the parameter sweep is given in **Fig. 3(a)** and **(b)**. For the primary side coil, an overall diameter of up to 80 mm is allowed. For the secondary side coil, the maximum diameter is limited to 70 mm. The maximum coil coupling factor was evaluated for a minimum coil separation distance of $d_{\mathrm{c,min}} = 10\,\mathrm{mm}$ and ideal coil positioning (i.e. perfect concentric alignment). For both coils, a single layer litz wire winding is considered, with litz wire strand diameters ranging from 32 µm to 71 µm. The maximum realized quality factors for the primary and secondary side coil with respect to the operating frequency range of 0.1 MHz to 2.5 MHz are shown in **Fig. 3(c)-(d)** for the different litz wire strand diameters. As expected, the coil quality factor increases with increasing frequency and decreasing strand diameter. However, for each strand diameter there is an optimal operating frequency range.

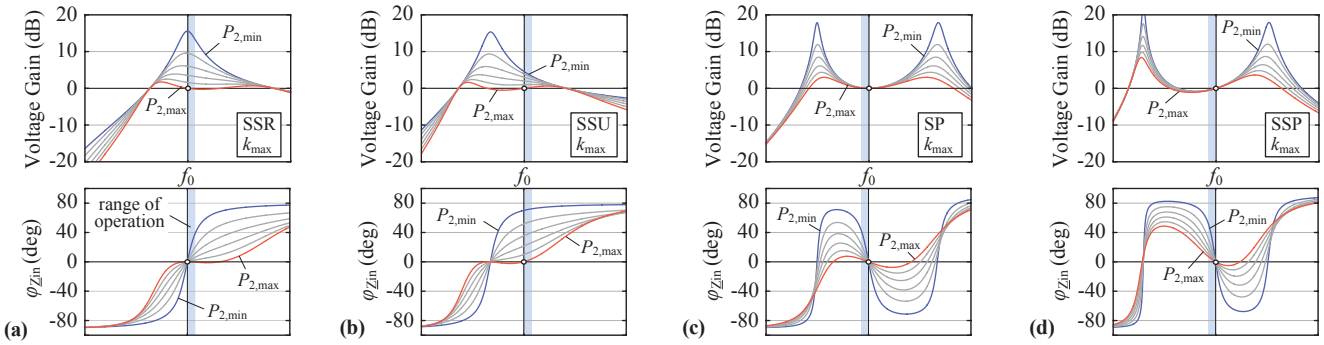

Figure 2: Voltage gain $G_\text{v}(\text{dB}) = 20\log_{10}\left(|\underline{u}_2/\underline{u}_1|\right)$ and phase angle of the input impedance $\varphi_{\underline{Z},\text{in}}$ of the series-series (SSR, SSU), series-parallel (SP) and series-series-parallel (SSP) compensated IPT systems, designed according to the equations provided in **Tab. I**.

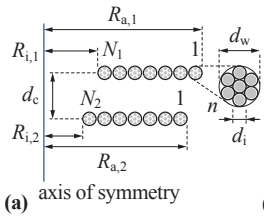

Coil Parameter		Value	
Prim. outer radius	$R_{\text{a},1}$	30, 35, 40	mm
Sec. outer radius	$R_{\text{a},2}$	25, 30, 35	mm
Min. inner radius	$R_{\text{i,min}}$	5	mm
Min. coil distance	$d_{\text{c,min}}$	10	mm
Number of strands	n	200, 250, 320	
Strand diameter	d_i	32, 40, 50, 71	µm
Frequency	f_0	0.1 - 2.5	MHz

(b)

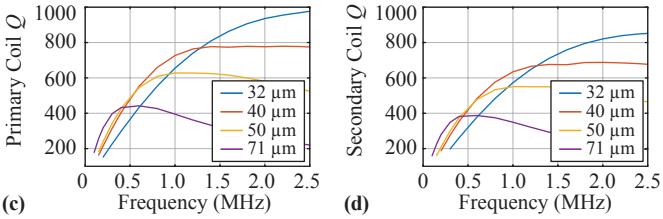

Figure 3: (a) Parameter range and designations used to generate the IPT coil sets. (b)-(c) Maximum primary and secondary side coil quality factors.

On the primary side, higher quality factors can be achieved because the maximum feasible coil diameter is larger than the maximum secondary side coil diameter, which allows for higher inductance values.

With the calculated values for the primary and secondary side inductances, AC resistances and maximum coil coupling factor, the design equations provided in **Tab. I** are used in a next step to design an IPT system for each coil set and topology, such that the maximum transmission efficiency is achieved at the maximum output power and maximum coil coupling factor, i.e. with zero phase angle of the input impedance and an ideal operation of the primary side inverter (i.e. no hard-switching).

However, in order to calculate the maximum power loss in each coil, the coil currents i_1 and i_2 must be known, whereby the rectifier circuit must be considered for an accurate calculation, as it will be shown in the following section.

B. Load Modeling

At a low coil coupling factor, the IPT resonant circuit acts as a bandpass filter with narrow bandwidth (for strong coupling pole splitting [14], [23] occurs). Hence, the impedance seen at the input of the resonant tank rises asymptotically with 20 dB/dec above the resonant frequency. Therefore, the high frequency harmonic content of the rectangular voltage waveform generated by a class-D inverter and/or the induced voltage in the secondary side coil is damped significantly such that the primary and secondary side coil currents i_1 and i_2 are almost perfectly sinusoidal in shape [17]. According to [24], for the series-series compensated system, a very simple equivalent load model can be used to model the load together with the full-wave rectifier, as shown in **Fig. 4(a)**. This model assumes a purely sinusoidal secondary side coil current, an ideal rectifier and a constant output voltage $U_{\text{DC},2}$. Consequently, the equivalent load resistance can be described with

$$R_{\text{L,eq,s}} = \frac{8}{\pi^2}\frac{U_{\text{DC},2}^2}{P_2} \,. \tag{3}$$

In the literature this simple load model is often used also for the case of the secondary side parallel compensated systems. However, it is only valid for the special case of a continuous sinusoidal current in the rectifier and does not apply to the SP and the SSP compensation with the rectifier circuit shown in **Fig. 4(b)**. Therefore, following the modeling approach presented in [25], a first harmonic model is used, where the rectifier circuit is replaced by an equivalent capacitance and equivalent load resistance based on the load dependent conduction time of the diode rectifier. As shown in **Fig. 4(c)**, assuming a sinusoidal secondary side coil current i_2, the parallel capacitance C_2 must be charged to the DC-link voltage $U_{\text{DC},2}$ at each zero crossing of i_2 in order to deliver the current i'_D to the load. Hence, the first harmonic of the rectifier's input voltage $u_{2,(1)}$ lags i_2 by a phase angle β, which represents a capacitive behaviour of the circuit. Starting with the calculation of the conduction angle θ of the bridge rectifier, which is given by

$$\theta = \arccos\left(\frac{2\omega_0 C_2 U_{\text{DC},2}^2 - \pi P_2}{2\omega_0 C_2 U_{\text{DC},2}^2 + \pi P_2}\right) \,, \tag{4}$$

the peak secondary side current $\hat{I}_2$ can be calculated with

$$\hat{I}_2 = \frac{\pi P_2}{U_{\text{DC},2}\left(1-\cos\left(\theta\right)\right)} \,. \tag{5}$$

Using the calculation of the first harmonic of the capacitor current $i_{\text{C2},(1)}$, the first harmonic of the rectifier input voltage $u_{2,(1)}$ can be obtained with

$$u_{2,(1)}(t) = \frac{1}{C_2}\int_0^t i_{\text{C2},(1)}(\tau)\text{d}\tau + c = \frac{\sqrt{a_1^2+b_1^2}}{\omega_0 C_2}\sin\left(\omega_0 t - \beta\right) \,, \tag{6}$$

and

$$\begin{aligned} a_1 &= \tfrac{\hat{I}_2}{\pi}\sin^2\left(\theta_\text{c}\right) \\ b_1 &= \tfrac{\hat{I}_2}{\pi}\left(\theta_\text{c} - \tfrac{1}{2}\sin\left(2\theta_\text{c}\right)\right) \\ \beta &= \arctan\left(\tfrac{b_1}{a_1}\right) \end{aligned} \,, \tag{7}$$

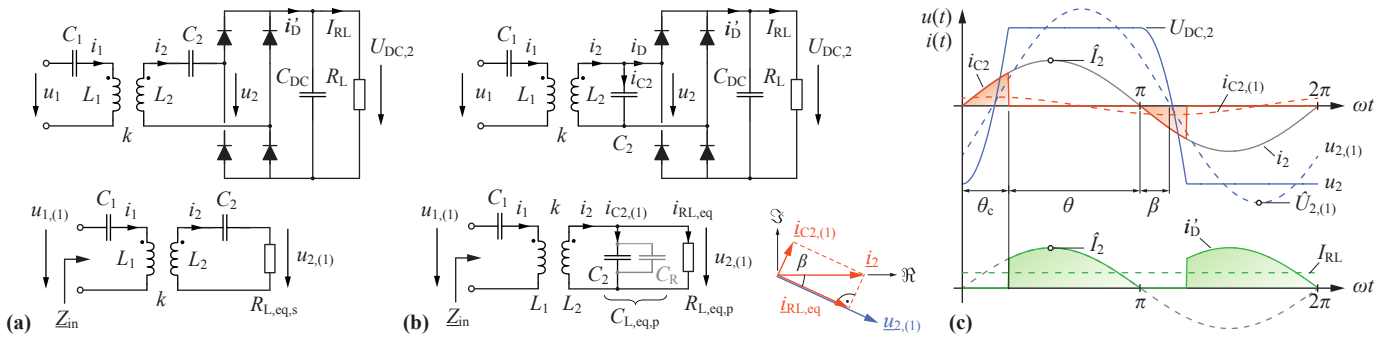

Figure 4: (a) Load model used for the series-series (SS) compensation method. (b) Load model used for the series-parallel (SP) and the series-series-parallel (SSP) compensation. (c) Secondary side current and voltage waveform in the case of secondary side parallel compensation.

where $\theta_c = \pi - \theta$ denotes the conduction angle of the parallel capacitor C_2. In the fundamental frequency equivalent model, the same power must be dissipated in the equivalent load resistance $R_{L,eq,p}$ as in the actual load resistance R_L. Hence, an equivalent resistive-capacitive load model can be obtained using the relations of the secondary side first harmonic voltages and currents depicted in the phasor diagram in **Fig. 4(b)**. The resulting equivalent load model is given by

$$R_{L,eq,p} = \frac{a_1^2 + b_1^2}{(\omega_0 C_2)^2 \, 2P_2} \quad \text{and} \quad C_{L,eq,p} = \frac{\tan(|\beta|)}{\omega_0 R_{L,eq,p}} \,. \tag{8}$$

As illustrated in **Fig. 4(b)**, the equivalent capacitance $C_{L,eq,p}$ is actually the parallel connection of the secondary side resonant tank capacitance C_2 and an additional load dependent capacitance C_R, which is due to the operation of the rectifier circuit.

Hence, it is important to note, that in the case of the secondary side parallel compensated IPT systems, the optimal output voltage and the secondary side compensation capacitance must be calculated iteratively, such that the equivalent load resistance $R_{L,eq,p}$ and the equivalent parallel capacitance $C_{L,eq,p}$ match the optimal values calculated with the design equations from **Tab. I**.

If the secondary side capacitance C_2 is decreased, the equivalent load resistance $R_{L,eq,p}$ converges to the simple load model given in (3). However, even a small parallel capacitance at the input of the rectifier, results in a much higher equivalent parallel capacitance, and hence, the peak secondary side coil current is underestimated with the simple model (3). Therefore, even for the modeling of a SS compensated IPT system, the enhanced load model can be used, in order to account for the parasitic capacitances of the rectifier diodes, as it was done for the power loss modeling of the SSU prototype system presented in [18].

In the next step, the primary and secondary side coil power losses are calculated and a numerical thermal model is used to find the thermal limitations of the TET system design.

C. Thermal Model

An axis symmetric two dimensional Finite Element (FE) thermal model similar to the model presented in [21] is used to calculate the tissue temperature. The structure of the model and the material properties used in the simulation are given in **Fig. 5**. The secondary side coil is embedded in the fat layer on top of the muscle tissue. The primary coil is covered by a clothing layer and is separated from the skin surface by a cotton fabric layer providing thermal insulation. The thermal properties of the textile materials are taken from [26]. For the convective heat transfer boundary B_{conv} a heat transfer coefficient of 2.5 W/(m^{2}K) [27] and an ambient temperature of 25 °C is assumed. For the remaining sides of the model, a thermal insulation boundary B_{iso} is used as indicated in **Fig. 5**. In the tissue material, Penne's bioheat equation [28] is solved to account for the heat generation and blood perfusion in the living tissue. The tissue material parameter are taken from [29] and for the arterial blood, a temperature of 36.8 °C is assumed. It is pointed out in [30], that the approximation used in Penne's bioheat equation of equal body core temperature and pre-arteriole blood temperature and the assumption of equal vein return temperature and local tissue temperature, both result in an overestimation of the effect of the blood perfusion on the local tissue temperature. Accordingly, the blood perfusion rate and in this case also the heat generation rate were used to calibrate the FE model, such that the temperature calculation matches the measured temperatures obtained from an animal experiment using the IPT coil set with the specifications given in **Fig. 7(d)**. And hence, for the thermal simulation, the blood perfusion rate and the metabolic heat source values shown in **Fig. 5** are scaled by a factor of 0.2 and 0.65 respectively.

In order to reduce the computation time for the temperature calculation for all IPT designs, the maximum tissue temperature is calculated for four combinations of the primary and secondary coil power loss [0,0], [$P_{loss,1}$,0], [0,$P_{loss,2}$] and [$P_{loss,1}$,$P_{loss,2}$]. Then, using the linearity of the thermal model, the maximum tissue temperature of any coil power loss combination can be calculated for the specific coil geometry, using linear interpolation. In order to allow for a variable coil geometry, an interpolation matrix is created with a coarse grid of the inside and outside coil radii, which significantly reduces the number of FE simulations. The maximum tissue temperature can then be calculated for each IPT system design and coil set in a post-processing step, using a six-dimensional linear interpolation function of the form

$$T_{tissue,max} = f(R_{a,1}, R_{i,1}, R_{a,2}, R_{i,2}, P_{loss,1}, P_{loss,2}) \,. \tag{9}$$

In order to comply with the regulations provided in [31] for active implantable medical devices, the surface temperature of the implanted coil must not exceed a temperature of more than 2 °C above the body core temperature of 37 °C. The threshold temperature for permanent tissue damage is approximately 42 °C [32], which is used as the absolute maximum thermal limit.

In the following section, the different IPT resonant circuit topologies are compared regarding the coil power losses and the thermal limitations due to the heating of the tissue.

D. Topology Comparison Results

According to the previous design strategy, for each coil set and resonant circuit topology, an IPT system is designed with maximum

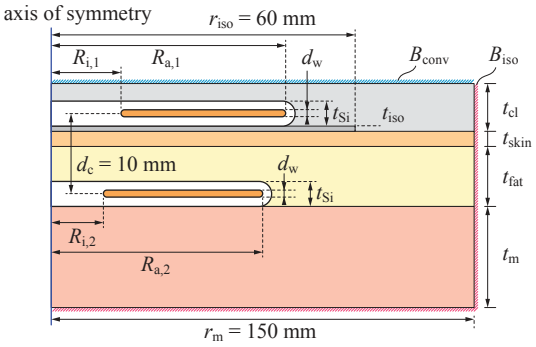

Parameter / Material		Length (mm)	Thermal Conductivity (W/m/K)	Density (kg/m^3)	Specific Heat (J/kg/K)	Blood Perfusion Rate (1/s) [1)]	Metabolic Heat Source (W/m^3) [2)]
Blood		-	0.52	1050	3617	-	0
Muscle	t_m	60	0.49	1090	3421	0.000672	991.9
Fat	t_{fat}	8.1	0.21	911	2348	0.000501	464.61
Skin	t_{skin}	1.4	0.37	1109	3391	0.001959	1829.85
Silicone	t_{Si}	3	0.23	1100	1300	-	-
Insulation	t_{iso}	0.5	0.026	327	1250	-	-
Clothing	t_{cl}	5.5	0.034	353	1250	-	-
Copper	d_w	1	400	8700	385	-	-

1) the blood perfusion rate values are scaled by a factor of 0.2 in the simulation
2) the methabolic heat source values are scaled by a factor of 0.65 in the simulation

Figure 5: Structure of the thermal simulation model and model parameters used for the temperature estimation in the human tissue.

energy transmission efficiency at operating frequencies in a range of 100 kHz to 2 MHz and a maximum power transmission of $P_{2,\max} = 30\,\mathrm{W}$. Accordingly, all IPT system designs show a purely resistive input impedance at the maximum output power and an inductive behaviour at all power levels below $P_{2,\max}$ and coupling factors below the maximum achievable value $k_{\max}$. In a second step, the power loss in each coil and the maximum tissue temperature are calculated, whereby a lossless rectifier circuit is assumed. For the compensation capacitances, assuming high quality class-1 C0G (NP0) ceramic capacitors, a dissipation factor of $\tan(\delta) = 0.0005$ is used to calculate the capacitor power losses according to

$$P_{\mathrm{loss,C}} = \frac{\tan(\delta)}{\omega_0 C} I_{\mathrm{C,rms}}^2 \,. \tag{10}$$

Fig. 6(a) shows the optimal output voltage $U_{\mathrm{DC},2}$ or each IPT system design with respect to the total IPT resonant circuit power loss, which includes the power loss of the primary and secondary side coil and the compensation capacitances. The SSR system achieves the lowest total power loss, but suffers from large voltage gain variations if the coil coupling and the output power is changed. However, as shown in [19], when an increased control effort is feasible, the highest energy transmission efficiency can be achieved with the SSR system in the entire load and coupling factor range, when the IPT input voltage $U_{\mathrm{DC},1}$ and output voltage $U_{\mathrm{DC},2}$ are adjusted simultaneously in order to operate the resonant circuit always with the optimal equivalent load resistance. The SSU system offers a similar high power transmission efficiency at high output power, and achieves a high secondary side efficiency in the entire range of operation, but shows only moderate voltage gain variations as shown in [18]. The SP system can achieve the same performance as the series-series compensated systems, but at much higher output voltages exceeding 100 V, which is not feasible for the application at hand. At an output voltage below 40 V, the series-series compensated systems clearly outperform the secondary side parallel compensated systems.

Considering the thermal limit indicated in **Fig. 6(a)**, it can be concluded that considering all resonant circuit topologies without output voltage limitation and a coil separation distance of 10 mm, a maximum total resonant circuit power loss of approximately 750 mW is acceptable for the IPT resonant circuit, which corresponds to an efficiency of 97.5 %. Note that the results given in **Fig. 6(a)** include the power losses of the resonant capacitances as well. Hence, the total permitted power loss in the energy transfer coils is lower than 750 mW, as shown in **Fig. 6(b)**, where the primary coil power loss is shown with respect to the secondary side coil power loss. In addition, the output voltage $U_{\mathrm{DC},2}$ is limited to 35 V. A much higher DC-link voltage is not advantageous, since it increases the secondary side peak coil voltage and the switching losses in the subsequent hard-switched converter stages such as the battery charging controller and the inverter driving the pump motor of the LVAD. Hence, as shown in **Fig. 6(b)**, the SS compensated IPT topology achieves a lower power loss in the secondary side coil compared to the secondary side parallel compensated topologies and only few feasible designs remain for the SP and SSP system.

However, the better performance of the SS compensated systems comes at the expense of a much higher secondary side coil voltage compared to the SP system, which limits the feasible designs and raises questions about the patient safety regarding the exposure to the electromagnetic field in the vicinity of the energy transfer coils, which is addressed in [33].

In summary, the comparison shows that the secondary side series compensated systems outperform the parallel compensated systems at the power transfer level at hand. In addition, due to the continuous sinusoidal secondary side current i_2, a highly efficient synchronous rectifier circuit can be realized easily even for high operating frequencies up to the MHz range [18]. Moreover, the secondary side parallel compensated systems suffer from high reactive power circulating in the secondary side resonant circuit, which further decreases the secondary side coil performance at partial load.

Hence, in the following section, the SS compensated topology is evaluated in more detail regarding the operation of the IPT system and the power conversion efficiency using measurements taken with the hardware prototype presented in [18].

III. IPT System Operation

The highest power transfer efficiency can be achieved with the SSR system if the output DC-link voltage is varied such that the optimal equivalent load resistance $R_{\mathrm{L,opt}}$ is present to the resonant circuit at any power delivered to the load and any coil coupling factor. This principle of operation is referred to as *efficiency optimal control* and is described in detail in [19]. A brief summary will be given in the following.

If the compensation capacitances are chosen according to the equations provided **Tab. I** for the SSR system and assuming a lossless operation of the resonant circuit and sinusoidal primary and secondary side coil currents, the power delivered to a resistive load is given by

$$P_2 = \frac{1}{2} \underbrace{\omega_0 L_{\mathrm{h}} \hat{I}_{1,(1)}}_{\hat{U}_{2,(1)}} \hat{I}_{2,(1)} = \frac{1}{2} \frac{\hat{U}_{1,(1)} \hat{U}_{2,(1)}}{\omega_0 L_{\mathrm{h}}} \,. \tag{11}$$

Note that in this case, the primary side coil current is 90°phase shifted with respect to the secondary side coil current. Assuming a

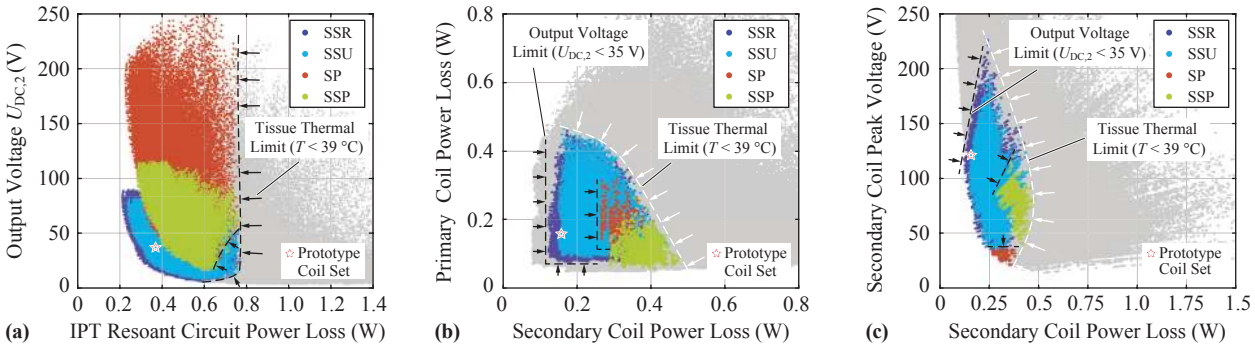

Figure 6: Comparison of the considered IPT resonant circuit topologies for maximum power transfer and maximum coil coupling, including the indicated prototype IPT coil set with the specifications given in **Fig. 7(d)**, operated as SSU system. (a) Calculated total power loss. (b) Calculated primary and secondary side coil power loss, when the system output voltage is limited to 35 V. (c) calculated secondary side coil peak voltage with respect to the secondary side coil power loss with the same output voltage limitation.

lossless inverter, a secondary side full-wave rectifier stage and using $\hat{U}_{\mathrm{i},(1)} = \frac{4}{\pi} U_{\mathrm{DC,i}},\ i \in [1,2]$, the equation for the output power can be expressed with

$$P_2 = \frac{8}{\pi^2} \frac{U_{\mathrm{DC},1} U_{\mathrm{DC},2}}{\omega_0 L_{\mathrm{h}}} \,. \tag{12}$$

From the equation for the optimal load resistance for the SSR system given in **Tab. I** follows that the output DC-link voltage $U_{\mathrm{DC},2}$ must be chosen according to

$$U^*_{\mathrm{DC,2,SSR}} = \sqrt{\frac{\pi^2}{8} P_2 k \omega_0 L_2} \,, \tag{13}$$

in order to provide load matching for any output power and coil coupling factor. The input DC-link voltage $U_{\mathrm{DC},1}$ is then determined by (12). **Fig. 7(a)-(c)** show the measured primary and secondary side DC-link voltages, the phase angle of the input impedance $\varphi_{\underline{Z},\mathrm{in}}$ and the DC-to-DC power conversion efficiency for the optimal operation of the SSR system using the hardware prototype shown in **Fig. 7(h)** with the synchronous rectifier circuit presented in [18]. The operating conditions and the component values of the resonant circuit are provided in **Fig. 7(d)**. **Fig. 7(a)** shows the adaptation of the output voltage according to equation (13) with respect to the output power at a coil separation distance of 10 mm and 20 mm. As a result, shown in **Fig. 7(b)**, the phase angle of the input impedance is almost constant with respect to the output power with a value between 11°and 19°, depending on the coil separation distance. The DC-to-DC power conversion efficiency is calculated from the measurement of the input and output current and voltage using Agilent 34410A multimeters and the results are shown in **Fig. 7(c)**. Note that the constant power loss of 258 mW due to the primary side FPGA is not included in the efficiency measurement. At a coil separation distance of 10 mm, the relative error for the measured total power loss is ±0.34 % at 5 W output power and ±0.2 % at 30 W output power. A maximum DC-to-DC efficiency of 96.9 % is achieved at the minimum coil separation distance of 10 mm and is larger than 92 % even for a coil separation distance of 20 mm. At an output power of 5 W and 20 mm coil separation distance, this is an efficiency improvement of 6.6 %, compared to the SSU system operation with constant output voltage [18].

In order to ensure the efficiency optimal control, the coil coupling factor k in (13) needs to be estimated [19], e.g. by evaluating equation (11) using measurements of the output power and the primary and secondary side peak coil currents. However, if the communication between the primary and secondary side is interrupted, a load variation can result in a very high voltage at the output of the SSR system due to its large voltage gain, which raises questions about the controllability and operational safety. In addition, since the input and output voltage vary over a wide range above and also below the nominal primary and secondary side battery voltage range of 12-16.8 V, a buck-boost type DC-DC converter is needed on the primary and secondary side as illustrated in **Fig. 8(a)**, in order to provide the load matching. In this case, the voltage of the motor inverter is limited to the battery voltage and during the battery charging process, the full power needs to be supplied by the buck-boost converter as indicated in **Fig. 8(a)**. Hence, the inductor for the buck-boost converter needs to be designed for the maximum power rating and a large inductor volume is needed to reduce the power loss in the implant.

In summary and despite the impressive performance, the main disadvantages of the SSR system operation using efficiency optimal control is the increased control effort, the increased size of the power electronic circuit needed for the implant and the fact that the secondary side coil power loss is increasing with decreasing coil coupling factor, which increases the heating of the tissue at large coil separation distances. Therefore it is believed that the described SSR system operation is not the optimal solution for the application at hand.

It was shown in [18], that the SSU system operation with constant output voltage provides a high DC-to-DC efficiency at maximum output power. However, the partial load efficiency is decreased significantly due to the highly inductive input impedance and thus due to the increasing primary side RMS coil current. Therefore, similar to the efficiency optimal control explained above, it is proposed to allow for a variation of the secondary side DC-link voltage according to the output power demand, but without the need for coupling factor estimation.

For the SSU system, in order to allow for Zero-Voltage-Switching (ZVS) of the primary side inverter stage, the phase angle of the input impedance $\varphi_{\underline{Z},\mathrm{in}}$, which is given at the operating frequency ω_0 by

$$\varphi_{\underline{Z},\mathrm{in}} = \arctan\left(\frac{k_0 \left(R^2_{\mathrm{L,eq,s}} + \left(k_0^2 - k^2 \right) \omega_0^2 L_2^2 \right)}{k^2 \omega_0 L_2 R_{\mathrm{L,eq,s}}} \right) \,, \tag{14}$$

must be positive. Hence, as shown in [18], the SSU system needs to be designed for a design coupling factor k_0 such that

$$k_0 \geq \frac{k_{\max}}{\sqrt{3}} \,. \tag{15}$$

applies. In order to design the system for a desired input phase angle $\varphi_{\underline{Z},\mathrm{in,d}}$, large enough to ensure ZVS operation at maximum output

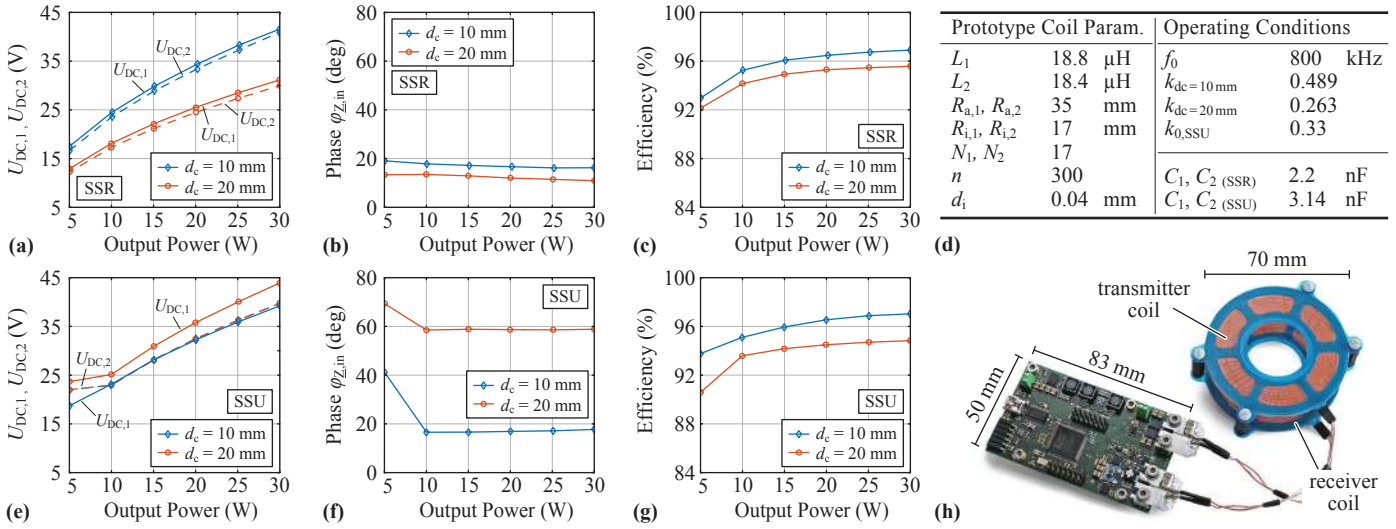

Prototype Coil Param.			Operating Conditions		
L_1	18.8	µH	f_0	800	kHz
L_2	18.4	µH	$k_{dc=10\,mm}$	0.489	
$R_{a,1}$, $R_{a,2}$	35	mm	$k_{dc=20\,mm}$	0.263	
$R_{i,1}$, $R_{i,2}$	17	mm	$k_{0,SSU}$	0.33	
N_1, N_2	17				
n	300		C_1, $C_{2\,(SSR)}$	2.2	nF
d_i	0.04	mm	C_1, $C_{2\,(SSU)}$	3.14	nF

Figure 7: (a)-(c) Measured input and output voltage, phase angle of the input impedance and DC-to-DC power conversion efficiency of the SSR system operation. (d) resonant circuit parameter used for the measurements. (e)-(g) Performance measurements of the SSU system operation. The measurement are carried out using the hardware prototype in (h) together with the secondary side synchronous rectifier described in [18]. Note that the constant power losses of 258 mW due to the primary side FPGA and auxiliary power supplies are not included in the efficiency measurement.

power and maximum coil coupling, the design coupling factor k_0 is determined by

$$k_0 = \frac{k_{\max}}{\sqrt{3}} \sqrt{\tan\left(\varphi_{\underline{Z},\mathrm{in,d}}\right)\sqrt{2}+1}\,. \tag{16}$$

Accordingly, the primary and secondary side compensation capacitors can be determined using the design equations provided in **Tab. I**. The secondary side DC-link voltage is then varied according to the power demand of the load using the equation [18]

$$U^*_{\mathrm{DC,2,SSU}} = \frac{2^{3/4}}{4}\pi\sqrt{P_2 k_0 \omega_0 L_2}\,. \tag{17}$$

The proposed structure and the control of the SSU system is shown in **Fig. 8(b)**. The power consumption of the LVAD and the battery charger is measured and the output voltage of the IPT system is calculated using equation (17). On the primary side of the system, a DC-DC converter is used to control the secondary side DC-link voltage $U_{\mathrm{DC},2}$. By using a lower limit for the secondary side DC-link voltage of 22 V, the buck-boost converter on the secondary side can be omitted and on the primary side a simple boost converter is used. Hence, as shown in **Fig. 8(b)**, the inverter and the buck-type battery charging controller are connected in parallel to the secondary side DC-link. The inductor used for the charging controller can then be designed for a lower power throughput and therefore occupies a smaller volume compared to the inductor needed for the secondary side buck-boost converter topology shown in **Fig. 8(a)**. Note that an upper voltage limit might be needed as well in order to reduce the secondary side peak voltage and the power losses in the subsequent converter stages.

The experimental verification is again based on the hardware prototype shown in **Fig. 7(h)** and the IPT resonant circuit components provided in **Fig. 7(d)**. **Fig. 7(e)** and **(f)** show the measured input/output DC-link voltages and the phase angle of the input impedance for the proposed SSU system operation respectively. With the control of the output voltage according to (17), the phase angle is constant with respect to the output power and is increasing with larger coil separation distances. The measured DC-to-DC power conversion efficiency is

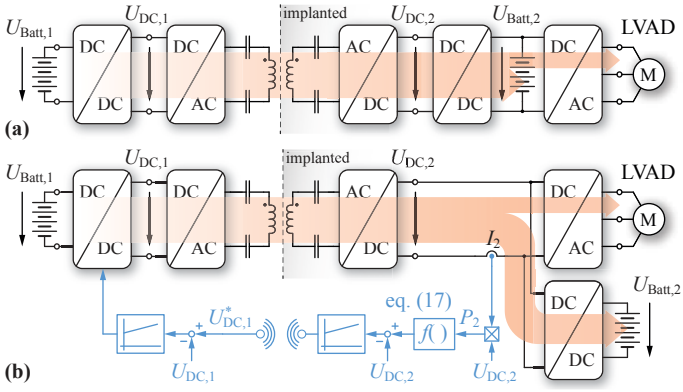

Figure 8: (a) TET system structure using the efficiency optimal control for the SS compensated IPT system operated at resonance [19]. (b) Proposed TET system structure and control for the SSU system operation, i.e. near the frequency for load independent voltage gain.

shown in **Fig. 7(g)**. At minimum coil separation, the efficiency is almost equal to the SSR system using the efficiency optimal control and reaches a maximum of 97 %. At a coil separation distance of 20 mm, the efficiency at minimum and maximum output power is 1.6 % and 0.75 % lower compared to the SSR system operation and above 90 % in the entire range of operation.

IV. Conclusions

In this paper, a comparative evaluation of three commonly used IPT resonant circuit topologies is conducted using both numerical and analytical models. The paper provides general IPT design guidelines and the models needed for the feasibility assessment of a high power TET system. The comparison shows that the series-series compensated topology outperforms the secondary side parallel compensated topologies in terms of secondary side coil power loss, especially if the output voltage of the IPT system is limited by the application. Measurements verify that the series-series compensated system operated at the resonant frequency (SSR) using efficiency optimal control

achieves the highest power conversion efficiency in the coil coupling and output power range, but requires a higher complexity of the control system. The operation near the frequency for load-independent voltage gain (SSU) using load impedance control offers similar performance at high and moderate coil coupling factors, but suffers from large reactive power on the primary side at low coil coupling, which limits the power transfer capability at large coil separation distances. On the other hand, the SSU system allows for a simplified control scheme without the need for coil coupling estimation and a reduced hardware complexity. In addition, in the case of an interruption or failure of the wireless communication, the SSU system benefits from the significantly lower voltage gain, which increases the functional safety of the TET system. Furthermore, in contrast to the SSU system, the secondary side coil power loss of the SSR system using the efficiency optimal control is increasing significantly at maximum output power and decreasing coil coupling factor, which increases the heating of the human tissue. Therefore, it can be summarized that the SSU system using load impedance control is a promising solution for the high power TET system application at hand. The achieved DC-to-DC power conversion efficiency is larger than 90 % in the entire operating range and reaches a maximum of 97 % using energy transfer coils with a diameter of 70 mm, a coil separation distance of 10 mm and ideal coil alignment.

ACKNOWLEDGMENT

The authors gratefully acknowledge the financial support by the Baugarten foundation. This work is part of the Zurich Heart project under the umbrella of "University Medicine Zurich/Hochschulmedizin Zürich".

REFERENCES

[1] B. H. Trachtenberg, A. Cordero-Reyes, B. Elias, and M. Loebe, "A review of infections in patients with left ventricular assist devices: prevention, diagnosis and management," *Methodist DeBakey Cardiovascular Journal*, vol. 11, no. 1, pp. 28–32, 2015.

[2] J. C. Schuder, "Powering an artificial heart: birth of the inductively coupled-radio frequency system in 1960," *Artif. Organs*, vol. 26, no. 11, pp. 909–915, 2002.

[3] T. Pirbodaghi, C. Cotter, and K. Bourque, "Power consumption of rotary blood pumps: pulsatile versus constant-speed mode," *Artif. Organs*, vol. 38, no. 12, pp. 1024–1028, 2014.

[4] M. S. Slaughter and T. J. Myers, "Transcutaneous energy transmission for mechanical circulatory support systems: history, current status, and future prospects," *J. Card. Surg.*, vol. 25, no. 4, pp. 484–489, 2010.

[5] T. D. Dissanayake, "An effective transcutaneous energy transfer (TET) system for artificial hearts," Ph.D. dissertation, Inst. Bioeng., Univ. Auckland, Auckland, New Zealand, 2010.

[6] Q. Chen, S.-C. Wong, C. K. Tse, and X. Ruan, "Analysis, design, and control of a transcutaneous power regulator for artificial hearts," *IEEE Trans. Biomed. Circuits Syst.*, vol. 3, no. 1, pp. 23–31, 2009.

[7] L. Bai, H. Tang, J. Nan, and G. Xin, "Optimal design of the TET system for achieving maximum power transfer," in *Proc. Int. Conf. Biomed. Eng. Comput. Sci. (ICBECS)*, 2010, pp. 1–4.

[8] H. Miura, S. Arai, Y. Kakubari, F. Sato, M. Matsuki, and T. Sato, "Improvement of the transcutaneous energy transmission system utilizing ferrite cored coils for artificial hearts," *IEEE Trans. Magn.*, vol. 42, no. 10, pp. 3578–3580, 2006.

[9] E. Okamoto, Y. Yamamoto, Y. Akasaka, T. Motomura, Y. Mitamura, and Y. Nosé, "A new transcutaneous energy transmission system with hybrid energy coils for driving an implantable biventricular assist device," *Artif. Organs*, vol. 33, no. 8, pp. 622–626, 2009.

[10] Y. Fu, L. Hu, X. Ruan, and X. Fu, "A transcutaneous energy transmission system for artificial heart adapting to changing impedance," *Artif. Organs*, vol. 39, no. 4, pp. 378–387, 2015.

[11] W. Zhang, S.-C. Wong, C. K. Tse, and Q. Chen, "Analysis and comparison of secondary series- and parallel-compensated inductive power transfer systems operating for optimal efficiency and load-independent voltage-transfer ratio," *IEEE Trans. Power Electron.*, vol. 29, no. 6, pp. 2979–2990, 2014.

[12] I. Nam, R. Dougal, and E. Santi, "Optimal design method to achieve both good robustness and efficiency in loosely-coupled wireless charging system employing series-parallel resonant tank with asymmetrical magnetic coupler," in *Proc. IEEE Energy Convers. Congr. Expo. (ECCE USA)*, 2013, pp. 3266–3276.

[13] ——, "Optimal design method for series LCLC resonant converter based on analytical solutions for voltage gain resonant peaks," in *Proc. IEEE Appl. Power Electron. Conf. Expo. (APEC)*, 2013, pp. 1429–1437.

[14] C.-S. Wang, G. A. Covic, and O. H. Stielau, "Power transfer capability and bifurcation phenomena of loosely coupled inductive power transfer systems," *IEEE Trans. Ind. Electron.*, vol. 51, no. 1, pp. 148–157, Feb. 2004.

[15] E. Waffenschmidt and T. Staring, "Limitation of inductive power transfer for consumer applications," in *Proc. 13th Eur. Conf. Power Electron. and Appl. (EPE)*, 2009, pp. 1–10.

[16] K. Schuylenbergh and R. Puers, *Inductive Powering: Basic Theory and Application to Biomedical Systems*, 1st ed. New York, NY, USA: Springer Science, 2009.

[17] R. Bosshard, J. W. Kolar, J. Mühlethaler, I. Stevanović, B. Wunsch, and F. Canales, "Modeling and η-α-Pareto optimization of inductive power transfer coils for electric vehicles," *IEEE J. Emerg. Sel. Topics Power Electron.*, vol. 3, no. 1, pp. 50–64, 2015.

[18] O. Knecht, R. Bosshard, and J. W. Kolar, "High-efficiency transcutaneous energy transfer for implantable mechanical heart support systems," *IEEE Trans. Power Electron.*, vol. 30, no. 11, pp. 6221–6236, 2015.

[19] R. Bosshard, "Multi-objective optimization of inductive power transfer systems for EV charging," Ph.D. dissertation, Dept. Elect. Eng., Swiss Federal Inst. of Technol. Zurich (ETHZ), Zurich, Switzerland, 2015.

[20] R. Bosshard, J. Mühlethaler, J. W. Kolar, and I. Stevanović, "The η-α-Pareto front of inductive power transfer coils," in *Proc. 38th Annu. Conf. IEEE Ind. Electron. Soc. (IECON)*, 2012, pp. 4270–4277.

[21] O. Knecht, R. Bosshard, J. W. Kolar, and C. T. Starck, "Optimization of transcutaneous energy transfer coils for high power medical applications," in *Proc. 15th IEEE Workshop on Control and Modeling of Power Electron. (COMPEL*, 2014, pp. 1–10.

[22] J. Muehlethaler, "Modeling and multi-objective optimization of inductive power components," Ph.D. dissertation, Dept. Elect. Eng., Swiss Federal Inst. of Technol. Zurich (ETHZ), Zurich, Switzerland, 2012.

[23] R. Bosshard, U. Badstübner, J. W. Kolar, and I. Stevanović, "Comparative evaluation of control methods for inductive power transfer," in *Proc. Int. Conf. Renewable Energy Research and Applications (ICRERA)*, 2012, pp. 1–6.

[24] R. L. Steigerwald, "A comparison of half-bridge resonant converter topologies," *IEEE Trans. Power Electron.*, vol. 3, no. 2, pp. 174–182, 1988.

[25] G. Ivensky, A. Kats, and S. Ben-Yaakov, "An RC load model of parallel and series-parallel resonant DC-DC converters with capacitive output filter," *IEEE Trans. Power Electron.*, vol. 14, no. 3, pp. 515–521, 1999.

[26] S. B. Stanković, D. Popović, and G. B. Poparić, "Thermal properties of textile fabrics made of natural and regenerated cellulose fibers," *Polymer Testing*, vol. 27, no. 1, pp. 41–48, 2008.

[27] Y. Kurazumi, T. Tsuchikawa, J. Ishii, K. Fukagawa, Y. Yamato, and N. Matsubara, "Radiative and convective heat transfer coefficients of the human body in natural convection," *Build. Environ.*, vol. 43, no. 12, p. 2142–2153, 2008.

[28] H. H. Pennes, "Analysis of tissue and arterial blood temperatures in the resting human forearm," *J. Appl. Physiol.*, vol. 1, no. 2, pp. 93–122, 1948.

[29] The IT'IS Foundation Website (2016, Oct.), "Database of tissue properties." [Online]. Available: http://www.itis.ethz.ch/itis-for-health/tissue-properties/database/

[30] A. Zolfaghari and M. Maerefat, "Bioheat Transfer," Developments in Heat Transfer, M. A. Dos Santos Bernardes (Ed.), InTech, 2011. [Online]. Available: http://www.intechopen.com/books/developments-in-heat-transfer/bioheat-transfer

[31] International Organization for Standardization (ISO), "Implants for surgery - Active implantable medical devices - Part 1: General requirements for safety, marking and for information to be provided by the manufacturer". ISO 14708-1:2014, Geneva, Switzerland, Aug. 2014.

[32] R. C. Lee, G. Russo, and G. Kicska, "Kinetics of heating in electrical shock," *Ann. N. Y. Acad. Sci.*, vol. 720, pp. 56–64, 1994.

[33] O. Knecht and J. W. Kolar, "Impact of transcutaneous energy transfer on the electric field and specific absorption rate in the human tissue," in *Proc. 41th Annu. Conf. IEEE Ind. Electron. Soc. (IECON)*, 2015, pp. 4977 – 4983.